Effect of active cooling on the formation of IN718 microstructures in directed energy deposition additive manufacturing

Michèle Bréhier, Daniel Weisz-Patrault, Christophe Tournier

Effect of active cooling on the formation of IN718 microstructures in directed energy deposition additive manufacturing

Michèle Bréhier[a,b,*], Daniel Weisz-Patrault[b], Christophe Tournier[a]

[a] *Université Paris-Saclay, ENS Paris-Saclay, LURPA, 4 avenue des sciences, Gif-sur-Yvette 91190, France*
[b] *LMS, CNRS, École Polytechnique, Institut Polytechnique de Paris, F-91128 Palaiseau, France*

Abstract

Purpose – This paper focuses on laser metal powder directed energy deposition, which is used to repair parts or manufacture high-performance components. Fine and equiaxed microstructures are often targeted because of their homogeneous mechanical properties. However, doing so can only be done by either adjusting process parameters or using external actuators that necessitate additional equipment. This paper presents a method that circumvents these issues by using only the powder spray nozzle and inerting gas when the laser is switched off to actively cool the part without additional equipment.
Design/methodology:approach – Single-bead IN718 thin walls were produced with a unidirectional strategy, taking advantage of the return path to actively cool the part. Six different sets of parameters were chosen to cover the operating range of laser power and machine scanning speed.
Findings – Analysis of the EBSD maps of the walls highlights the impact of this active cooling strategy on the microstructure. A fine, untextured microstructure was observed, regardless of process parameters, which enables optimization of process parameters to maximize productivity instead of being conditioned by the targeted fine-equiaxed microstructure. The grain size obtained can be further refined by increasing the scanning speed of the actively cooled parts.
Originality – An informed choice of off-production nozzle trajectories would enable reaching a homogeneous microstructure independently of process parameters.

Keywords: Additive manufacturing ; Microstructure ; Electron Back Scattering Diffraction (EBSD) ; process parameters ;

1. Introduction

The family of additive processes known as metal Additive Manufacturing (AM) has received increasing attention over the years, since the geometry and material of the part, and therefore the microstructure, are produced simultaneously. These processes enable the achievement of previously unattainable geometries and properties for manufactured or repaired parts. Among AM processes [1], Directed Energy Deposition (DED) processes focus thermal energy to melt materials as they are deposited. These processes are particularly interesting for part repair and the manufacture of high-performance components [2]. Optimizing microstructure in AM is essential for developing components with enhanced performance, paving the way for parts with voluntarily non-homogeneous properties through microstructure control. To do so, the formation of microstructures in DED must first be studied as they directly influence the mechanical properties of the final material [3, 4].

*Corresponding author: *michele.brehier@ens-paris-saclay.fr*

Process parameters and manufacturing strategy influence cooling rates, temperature gradients, and melt pool shape [5], thus conditioning the part's microstructure (i.e., grain structure and solid state phase distribution) [6–8]. The microstructure is also affected by the various thermal cycles [9] caused by the heat source passing over a bead that has already been deposited [10], which, depending on the size of the melt pool, can lead to a remelting of the previous bead(s) [11]. Given typical temperatures and cooling rates of $10^2 - 10^6$(K/s) in DED [12], the microstructure morphology generally observed is columnar, cellular, or dendritic, and bands of equiaxed grains may appear depending on the process parameters.

Many studies have investigated the influence of various parameters on the microstructure formation. Material, laser power, and dwell time are the most significant parameters for controlling the microstructure. Depending on the material and the content in alloying elements, the microstructural properties are quite different [13]. For example, in the case of parts produced by Laser Metal Powder Directed Energy Deposition (LMP-DED), microstructural properties were analyzed for TiAl6V4 and IN718 [14]. By increasing the Nb content of nickel-based alloy, Ni et al. [15] refined the microstructure. Sargent et al. [16] have mixed IN718 and Stainless Steel 316L to achieve a finer microstructure both as-built and after heat treatment. For the same material, Parimi et al. [17] showed that by increasing the laser power, the microstructure changes from columnar with bands of equiaxed grains at the interlayers to an exclusively columnar, more textured microstructure with much larger grains. Chauvet et al. [18] came quite close to producing a single crystal by increasing laser power and decreasing scanning speed. By adding a dwell time to their bidirectional strategy, Guévenoux et al. [19] also produced two distinct microstructures, one highly textured and columnar, the other finer and untextured. Increasing the interlayer dwell time results in higher cooling rates, thus reducing grain size. The reduction of grain size then increases yield strength and tensile strength, which are also more uniform across the part [20].

Other process parameters influencing grain growth direction, size, and texture have also been studied. Bambach et al. [21] compared the nature of the feedstock material, showing that the use of IN718 powder results in grains that cross the layers, unlike IN718 wire, which may lead to recrystallization zones. The influence of the scan path strategy is also documented for a given process. For example, in the case of a single bead thin wall [22], the unidirectional strategy leads to grain nucleation in every layer, whereas the bidirectional strategy results in epitaxial growth following the secondary dendrite of the previous layer. This particular epitaxial growth leads to alternating grain inclination in every second layer.

For IN718 alloy cubes, Liu et al. [23] have shown that the cross-directional raster scanning strategy results in a finer microstructure than the single-directional raster one. The degree of overlap between two beads also influences the microstructure: the higher the overlap, the finer the grains [24]. Tests on a Co-based alloy by Ocelík et al. [25] showed that the grain shape ratio increases with scan speed. The laser intensity profile, studied by Bremer et al. [26], can lead to a more equiaxed microstructure by shifting from a circular to a square profile. The laser mode can also refine the microstructure using quasi-continuous waves [27]. However, these microstructure variations are less significant than those obtained by playing on the material, power, and dwell time.

Modifying the microstructure with process parameters is advantageous, in that doing so can obtain the locally best microstructure suited to the mechanical stresses on the part being produced. Modifying process parameters or using auxiliary fields associated with additive manufacturing (FAAM) such as magnetic [28], acoustic, or thermal fields [29] have been applied to numerous studies that aim to refine the microstructure and achieve a uniformly equiaxed distribution in order to homogenize mechanical properties. For example, adding ultrasonic vibration to assist LMP-DED manufacturing of IN718 parts reduced porosity and lowered average grain size [30]. Higher ultrasonic frequency results in smaller grains [31]. Zhou et al. [32] have shown numericaly that the addition of a magnetostatic field tends to stabilize the melt pool. Using laser remelting, Zhang et al. [33] were able to reduce grain size by increasing the speed of the laser.

Thus existing methods for obtaining a very fine, untextured microstructure, therefore, work either for a specific low-power recipe or require the addition of delays or extra equipment. Therefore, this work proposes a new approach to control the microstructure toward a fine untextured microstructure in LMP-DED that is based on active cooling of the beads just after metal deposition by scanning the part with the inert covering gas that carries the powder when the laser is switched off.

The effect of active cooling significantly impacts thermal gradients and cooling rates, which in turn may be sufficient to reach the columnar to equiaxed transition (CET) and form a larger fraction of equiaxed grains on the top

of the melt pool. The passage of the nozzle cools the last bead deposited, leading to a cooler melt pool and reducing the possibility of remelting the equiaxed grain band from the previous layer.

This approach has been tested on single-bead IN718 thin walls fabricated using LMP-DED. Unlike most existing studies, the proposed method does not necessitate fine-tuning of process parameters, as satisfying results are obtained regardless of process parameters. Another key advantage of the proposed work over the existing attempts to obtain fine untextured microstructures is that it relies only on the current LMP-DED machine without needing additional equipment.

The paper is organized as follows. First, the experimental design, consisting of six trials of varying parameters, and the scanning strategy are presented in section 2. Then, results, particularly the macroscopic and microstructural effects, are analyzed in detail in section 3. Finally, the contribution of active cooling for the different parameters and results from the literature are discussed in section 4, and conclusive remarks are provided in section 5.

2. Materials and methods

2.1. Experimental setup

A total of 6 single bead thin walls were manufactured on a 5-axis BeAM™Mobile machine equipped with a type 10Vx nozzle, including a powder jet, a local argon supply (i.e., inert cover gas), and a 500 W fiber laser source from IPG™with an operational range of 200-400 W. The thin walls are 40 mm long and 30 mm high, and their thickness ranges from 0.8 mm to 1.1 mm depending on process parameters. All walls were built on the same 10 mm-thick steel substrate. The powder used was IN718, a nickel-iron alloy with the following nominal composition: 50–55 wt% of Ni, 17–21 wt% of Cr, 4.8–5.5 wt% of Nb, 2.8–3 wt% of Mo, 0.65–1.15 wt% of Ti, 1 wt% of Co, small additions of Al (0.2–0.8 wt%), and Fe (balance) [34]. The morphologies and properties of the powder used are the same as in [35].

Waterjet cutting was utilized to extract 15 mm $\times$ 15 mm samples from the central area of each wall. The microscopic study of the walls was conducted using a focus variation microscope IF-Sensor R25 with an x5 optical zoom. The area observed was 3.5 mm $\times$ 3.5 mm. The samples were heat-coated in a conductive resin to achieve mirror polishing up to 1 µm. They were later electrochemically etched with orthophosphoric acid at 5V for 10 seconds. For electron back-scatter diffraction (EBSD) analysis, a FEI Quanta 600 FEG-ESEM Scanning Electron Microscope (SEM) was used in this study. The EBSD maps were acquired through the Aztec software with a step size of 0.9 µm, and the beam voltage was set to 25 kV. Channel 5 software was used to plot the EBSD maps. Each grain was identified by imposing a disorientation threshold of 10° for defining grain boundaries.

2.2. Process parameters

The following process parameters are chosen following the design experiment proposed in [36]. The powder flow rate is set to 9 g/min for the entire experimental design. Scanning speed and laser power vary within the operating range of the BeAM™machine. Scanning speed varies from 1125 mm/min to 2625 mm/min, and laser power from 250 W to 350 W. In this study, 4 different scanning speeds denoted by V are considered (namely 1125, 1875, 2250, and 2625 mm/min) as well as 3 different laser powers denoted by P (namely 250, 300, and 350 W). These process parameters are combined to perform 6 experiments, including different scanning speeds for the same power, different powers for the same scanning speed, and three tests with the same linear energy (i.e., P/V ratio). The resulting (P, V) diagram is presented in figure 1, where the indexes correspond to the names of the walls in the following.

2.3. Active cooling

The scanning strategy used to create the walls is unidirectional. This means the nozzle only deposits material on the forward path while the return path is laser-off. The special feature of this strategy is that the return path is on the same plane as the forward path but the nozzle is offset in Z (i.e., the build direction) by the height required to produce the next bead. To maintain powder flow control, it is common practice in the LMP-DED to never switch off the powder spray during manufacture, even when the laser is switched off. Consequently, the part being produced is actively cooled down by the supply gas and, the cover gas on the way back of the nozzle. The powder flow rate is

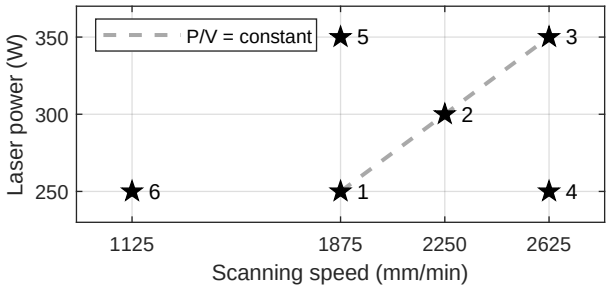

Figure 1: Process parameters for the six thin walls of the experimental design.

maintained at a constant 9 g/min, supplied by argon. The gas flow rates depend on the nozzle used, in this case, the 10 Vx. The central gas flow rate is 3.0 l/min and, the secondary gas flow rate is 6.0 l/min during the entire production process, with the laser on or off. The sum of these two gas flows, combined with the powder blown on the return path of the nozzle constitutes the active cooling. A schematic representation of this active cooling strategy with forward and return nozzle paths is shown in Figure 2. It should be noted that the nozzle speed on the return path is 2250 mm/min, whatever the wall parameters. Considering the proposed scanning strategy, it is clear that at a given point, the time between bead deposition and active cooling with the nozzle return varies linearly along the wall length direction, as shown in figure 3. Microstructure analyses are carried out on specimens extracted in the central zone of the wall, represented by the two vertical lines in figure 3. Within this central zone, the time between bead deposition and active cooling is, therefore, rather uniform for the different walls. It ranges from 0.9 s for walls with the highest scanning speed (i.e., 2625 mm/min) to 1.7 s for those with the lowest scanning speed (i.e., 1125 mm/min).

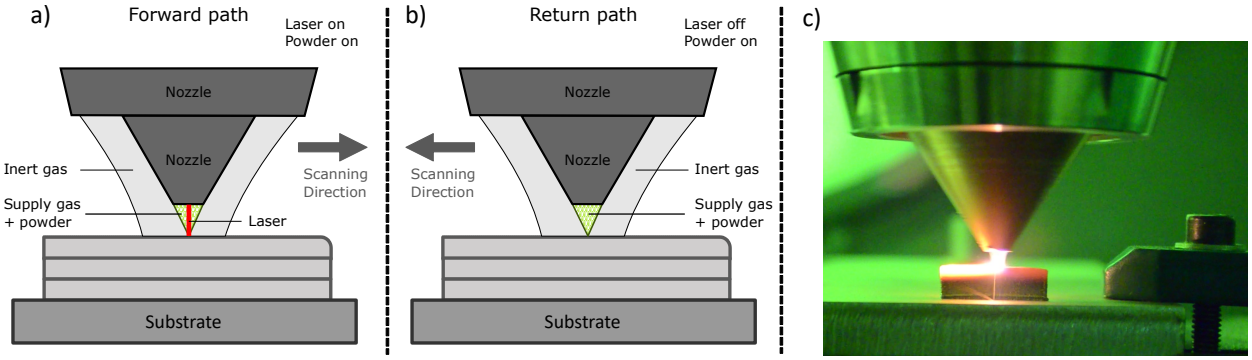

Figure 2: Schematic representation of the active cooling strategy with forward (a) and return nozzle paths (b) and a picture of a wall being produced (c)

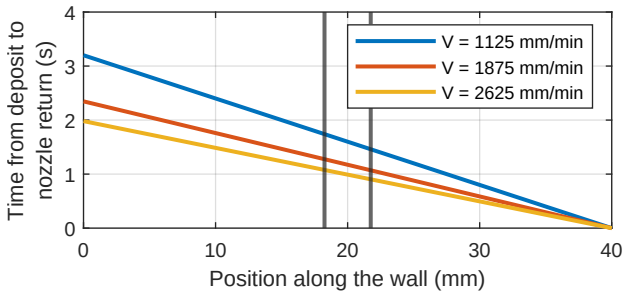

Figure 3: Time from deposit to nozzle return for the different scanning speed.

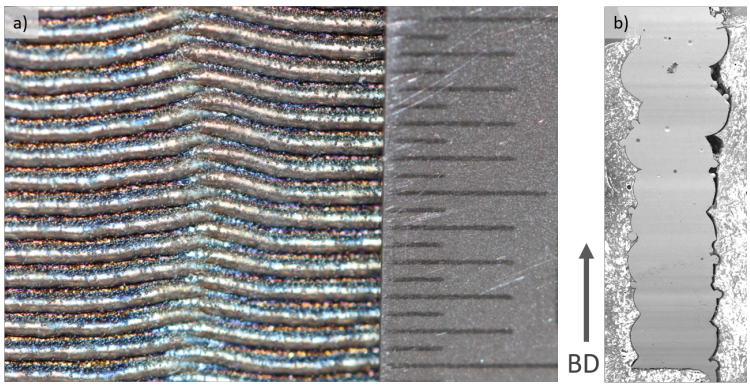

Figure 4: Picture of staggered stack inversion and propagation on wall 6 in (a) longitudinal view with a measuring instrument whose graduations correspond to 0.5 mm, and (b) cross section view.

3. Results

3.1. Macroscopic considerations

First, the overall aspect of the produced walls is examined. The analysis shows that, depending on the process parameters, three types of stacking can be observed: stacking beads on top of each other, staggered stacking, and chaotic stacking. It's worth noting that this observation is repeatable, with the same parameters producing the same type of stacking several times over.

One could think that the active cooling may be responsible for staggered and chaotic stacking patterns. Still, similar issues have already been observed in the literature for walls fabricated with a bidirectional strategy without active cooling [14]. Therefore, defects in stacking patterns cannot be attributed to active cooling but rather to a combination of process parameters. It has been shown that changing the process parameters allows switching from one type of stacking to another for the same nozzle.

Staggered and chaotic stacking patterns may result from fluid instability, leading to the deposition of an asymmetrical bead. The following bead will then spread non-symmetrically but on the opposite side, partially filling the space left by the previous bead. This phenomenon is amplified in the first layers to give the observed stabilized stacking regime. Depending on process parameters and the lateral offset of the melt pool, the asymmetry of the deposited bead changes - rarely, as in the case of staggered wall- or frequently, thus resulting in chaotic stacking. Figure 4 illustrates the inversion of the staggered stack pattern on wall 6 and the propagation of this inversion to subsequent layers. The asymmetry of the powder jet, visible in the difference in density of unmelted powder on the two faces of the same wall, could also destabilize the melt pool.

3.2. Microstructure analysis

A microstructure analysis is carried out on a 3.5 mm $\times$ 3.5 mm central zone of each wall, sufficiently high for a stable thermal regime to be established. The inverse pole figures (IPFs) in the building direction, in the plane of the walls, are shown in figure 5 for all the produced walls. The classic structure of LMP-DED shows a dendritic structure with both columnar and equiaxed grains. The grains are arranged so that one can identify the different layers and relate them to the three types of bead stacking that were previously identified. The columnar grains are tilted in the laser scanning direction and separated by small equiaxed grains, which correspond to the boundary with the next bead. A macrograph of wall 5 captured by the Alicona microscope is presented in figure 6(a), and an EBSD map colored according to grain size is shown in figure 6(b). Despite the chaotic stacking, there is a pattern of small equiaxed grains in the interlayer and columnar grains corresponding to the bead arrangement. None of the six analyzed walls showed consistent grain growth over multiple layers. However, it is possible to observe a few grains spreading over two layers for process parameters corresponding to regular stacking walls 1 and 4.

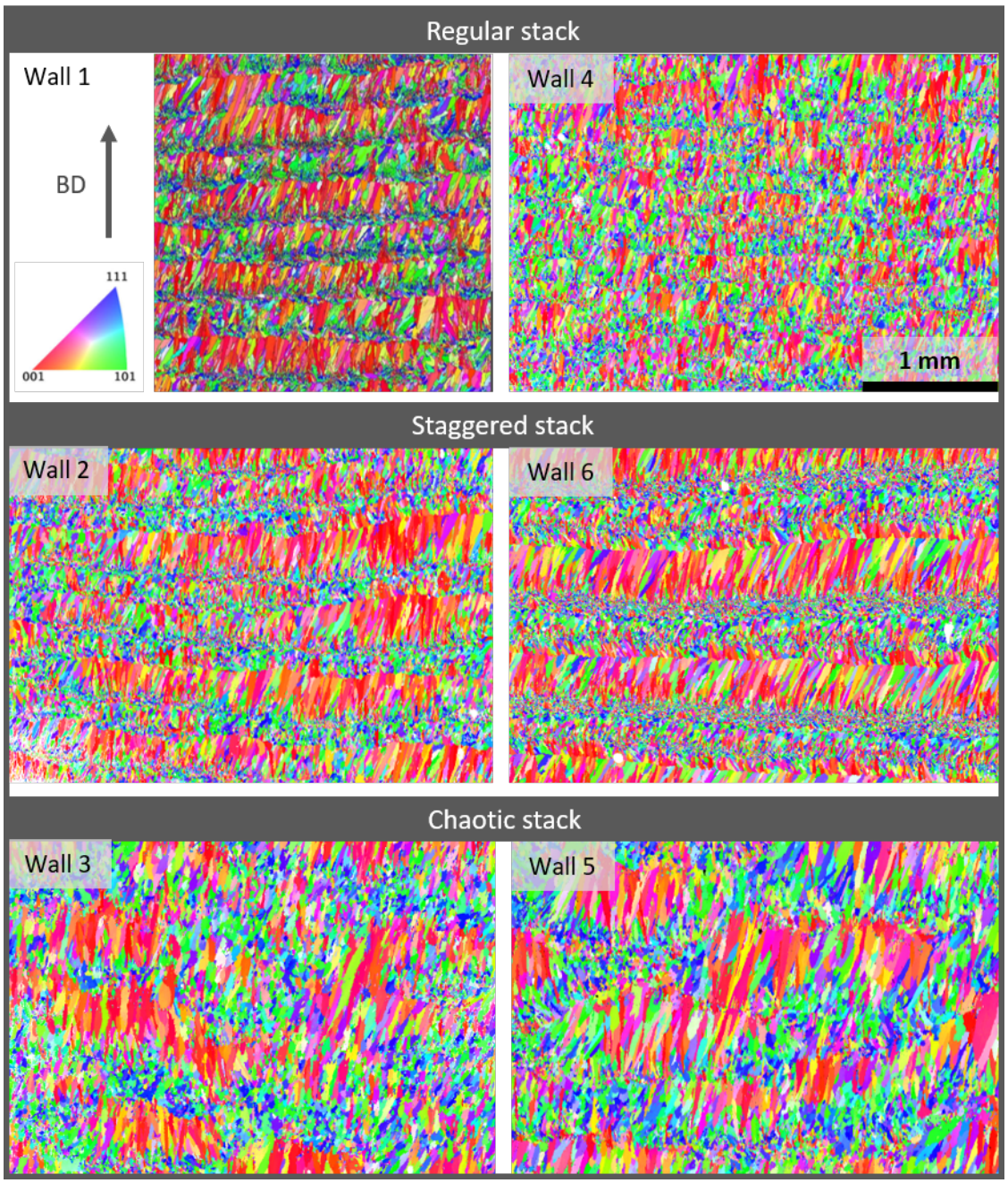

Figure 5: IPF in the building direction all six walls grouped by stacking type

To better understand and interpret the IPFs provided in figure 5, it is essential to consider the three-dimensional nature of the observed microstructures, especially for staggered and chaotic stacking patterns. For instance, in the case of the staggered stack, the microstructure revealed by EBSD maps depends on the position of the cutting plane with respect to the mid-plane of the bead. To illustrate this effect, a cross-sectional view diagram of a single-bead thin wall based on ellipses representing the grains is presented in figure 7. As reported by Guévenoux et al. [19] (using cross-sectional EBS maps), the columnar grains are oriented from the sides toward the mid-plane of the bead. Therefore, if the mid-plane of the bead is offset by around 0.1 mm, as observed, for instance, on wall 6, the inclined

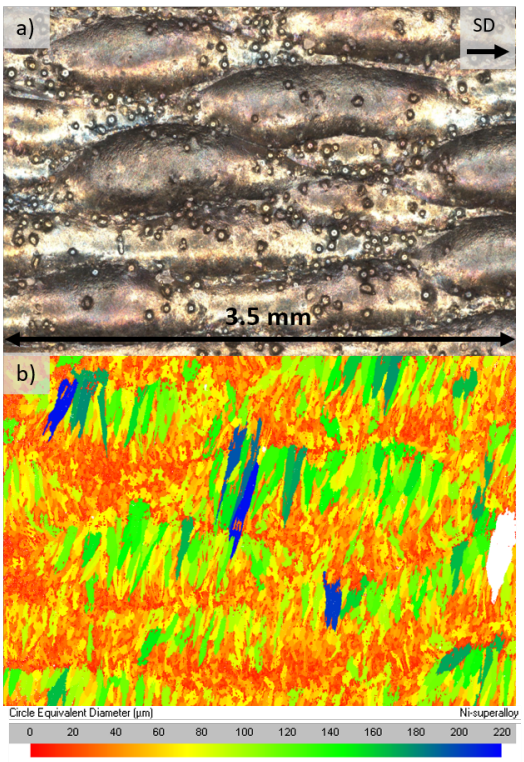

Figure 6: a) Macrograph of the observation zone, and b) EBSD map colored according to grain size.

grains are cut and appear less elliptical and smaller on the EBSD maps. Thus, when analyzing walls with staggered bead stacks using EBSDs, every second layer may seem to contain large equiaxed grains, whereas they are columnar grains cut with an offset from the mid-plane of the bead.

Based on these remarks, one can exploit the staggered stack pattern in some regions to obtain insights into the 3D arrangement of the microstructure. Indeed, a specific region in wall 6 is presented in figure 8a) where the alternating pattern between beads changes sides. The corresponding IPF is presented in figure 8b), where the observed cutting plane corresponds to different positions continuously evolving with respect to the bead mid-plane. Following each bead, one can, therefore, assess microstructure variations along the bead thickness as it is somehow spread from the mid-plane -where crystal directions [001] are oriented along the build direction Z- to a plane offset by 0.1 mm -where crystal orientations are distributed much more. This analysis emphasizes that the plane's position in which the EBSD is taken is crucial for representing the part's actual microstructure. This same reasoning applies to walls with chaotically stacked beads.

Aware of the limitations of studying microstructure in a single plane as significant variations have been evidenced along the bead thickness, comparing IPFs of different walls is still possible to address the relative impact of varying fabrication conditions on microstructures. In EBSD maps, the minimum grain size threshold is set to 5 pixels. On this basis and depending on the wall, the number of grains varies from around 16,500 (wall 5) to over 54,000 (wall 6). An ellipse approximates each grain to perform a quantitative analysis. In this way, grain size, shape, and inclination comparisons are carried out using ellipse parameters.

The average grain size over all grains of each wall ranges between 16 µm and 28.5 µm. The excessive presence of small grains about large columnar grains pulls the average downwards. Considering that a grain is regarded as a "large columnar grain" when the associated ellipse's major axis is higher than half a layer, the proportions of small grains are listed in table 1. It includes equiaxed grains and columnar grains with an offset of the cutting plane with respect to the mid-plane of the bead as evidenced in figure 7. The relative number of small grains is higher than 94% for the 6 walls, which explains the low average grain size. An essential feature of all the obtained microstructures is that the

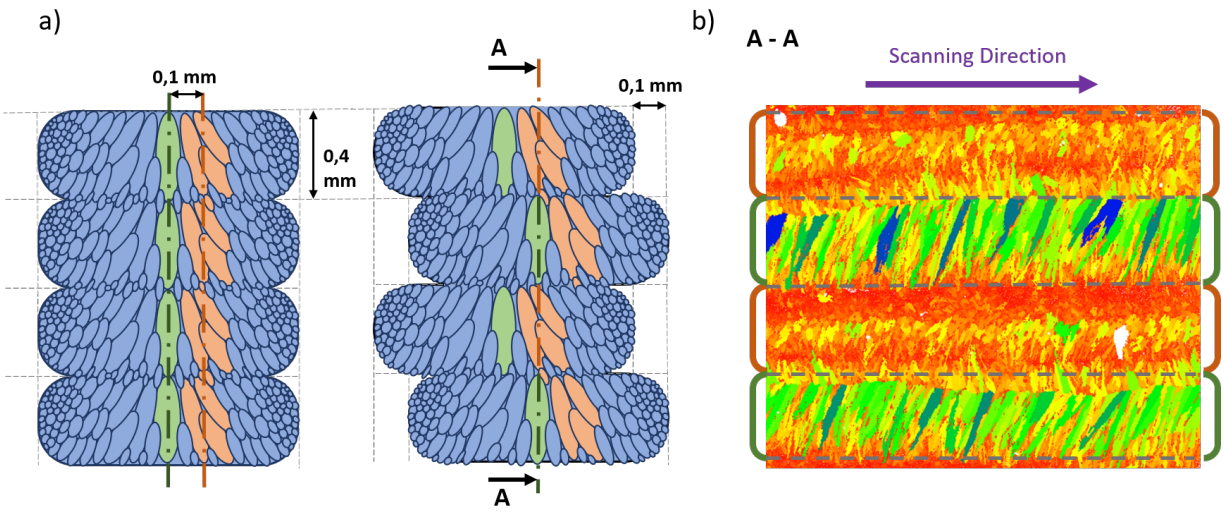

Figure 7: a) Illustration showing the impact of staggered stacking on the observed microstructure in the plane of wall b) corresponding EBSD map colored according to grain size showing that columnar grains may appear in full length on the EBSD map -when the cutting plane corresponds to the mid-plane of the layer- or much smaller -when the cutting plane is offset from the layer mid-plane.

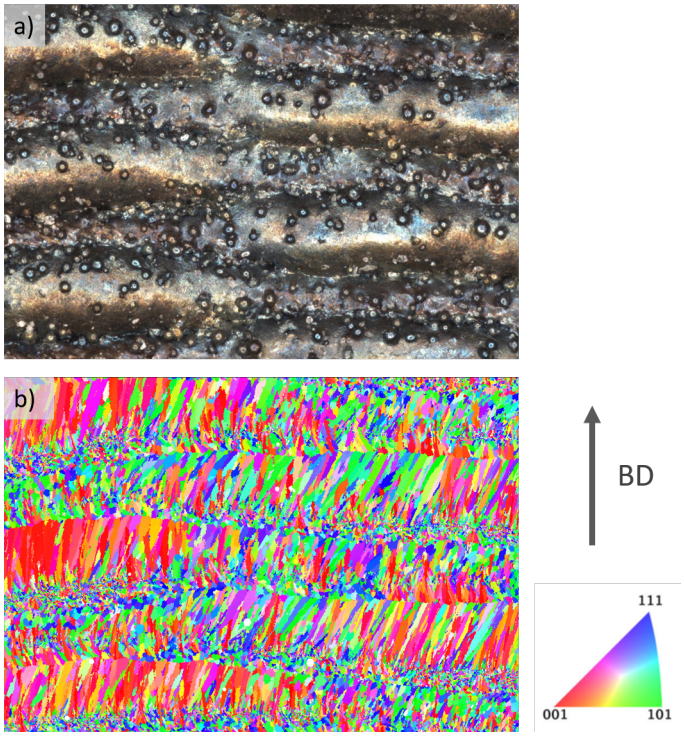

Figure 8: a) Macrograph of wall 6 showing the region where the alternating pattern changes sides. b) IPF of the same region

relative surface occupied by small untextured grains is significant, even though not all small grains are equiaxed.

Since small grains prevail in all grain statistics regardless of process parameters, only large columnar grains - filtered according to the criterion of size higher than half the bead height- are considered in the following to emphasize the effect of process parameters better. The grain size of large columnar grains is presented in figure 9, which reveals a

Wall	1	2	3	4	5	6
Number of grains	35205	36818	16898	41544	16476	54378
Mean size (µm)	21.1	20.6	28.4	20.3	28.5	16.2
Small grain ratio (%)	99.2	99	94.2	97.5	96.9	98.8
Small grain surface (%)	83	81	49	72	58	92

Table 1: Grain mean size and small grain proportion for the six walls

strong negative linear association with the scanning speed. This observation is shared whether considering an increase in speed at constant linear energy with walls 1, 2, and 3 or constant laser power with walls 1, 4, and 6. Increasing laser power slightly increases the average grain size for a given speed but to a much lesser extent than the scanning speed. This effect is only partly explained by the fact that since very few grains cross several layers, the size of large columnar grains is conditioned by the bead height, which depends on process parameters, and in particular, a negative association has been found between the bead height and the scanning speed [36].

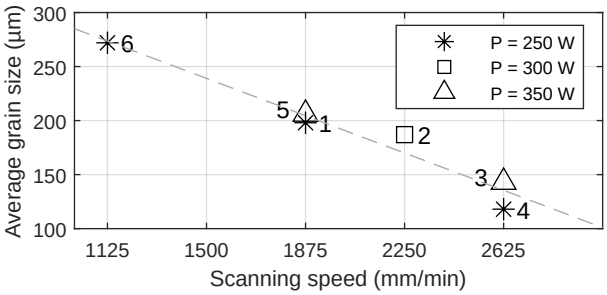

Figure 9: Evolution of average grain size as a function of scanning speed and laser power considering the large columnar grains

The tilt of the grains to the substrate also shows a speed-related trend at constant power. Thus, an increase in speed leads to an increase in the angle between the substrate and the grains. The higher the speed, the more vertical the grains. The average value of the angle thus formed varies from 70° for the lowest speed to 81° for the highest, for a power of 250 W. However, power does not seem to influence the tilt of the grains directly in the presented experiments.

Finally, in terms of crystallographic texture, as seen from the IPFs presented in figure 5, the samples all show a preferential crystalline grain orientation parallel to the (100) planes. This direction corresponds to that of fabrication, which is in line with what can be seen in the literature. However, as the maximum density values are between 3.3 and 5.2 × random, the walls can be described as lightly textured. As this observation applies to all walls, it is independent of process parameters.

4. Discussion

4.1. Influence of active cooling on microstructure

Among the microstructural characteristics presented above, the distinguishing feature with the literature lies in the systematic alternation of small equiaxed grains and columnar grains regardless of process parameters. As depicted in figure 10, thermal gradient G and solidification front rate R (i.e., the normal speed of the solidification front) significantly evolve along the solidification front, which may be sufficient to cross the columnar to equiaxed transition (CET) and, therefore, obtain columnar elongated grains along with equiaxed grains. Indeed, the thermal gradient G is, by definition, always aligned with the outer normal of the solidification front and is much higher in the build direction (i.e., vertical) than in the scanning direction (i.e., horizontal) [7]. In addition, on the one hand, when the outer normal of the solidification front is aligned with the scanning direction (blue marker in figure 10), R reaches its maximum (i.e., the scanning speed) and the thermal gradient G reaches its minimum (i.e., aligned with the scanning direction), which tend to favor the formation of equiaxed grains. On the other hand, when the solidification front outer normal is

perpendicular to the scanning direction (red marker in figure 10), R becomes negligible, and G reaches its maximum (i.e., aligned with the build direction), which tends to favor the formation of columnar grains. Active cooling tends to reduce the melt pool length, leading to lower thermal gradient G and higher solidification front velocity R at the top of the melt pool (i.e., blue marker in figure 10) because the outer normal of the solidification front is more aligned with the scanning direction. This leads to the formation of equiaxed grains as shown in figure 10.

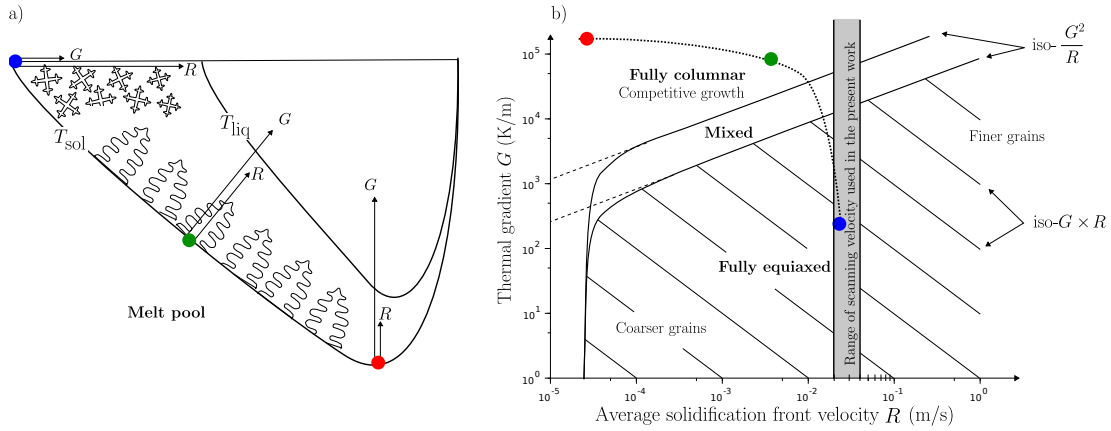

Figure 10: a) Schematic view of the melt pool with different isotherms and solidification regimes, and b) a solidification map for IN718 extracted from [37] enabling the determination of the solidification regime.

To demonstrate the specific effect of active cooling experimentally, a comparison can be made with the result presented by Guevenoux [38] as the machine is identical. In the case of Guévenoux et al. [19], the power used is the same as for walls 1, 4, and 6, and the scanning speed used is 2000 mm/min, i.e., between those of walls 1 and 4. The significant difference lies not in the parameters chosen but in the lasering strategy: bidirectional for Guévenoux et al. [19] and unidirectional with active cooling in this contribution. Considering the center of the walls, where the EBSD mapping was carried out, the time between two laser passes at the same point is similar in the cases of Guévenoux et al. [19] without delay and wall 4, of 2.7 s. Results are therefore comparable and presented in figure 11. The specific effect of active cooling is demonstrated, allowing a layer of small, equiaxed grains to form between each layer. In this way, the grains do not pass through the layers. This impacts the structure of the grains, which is then mixed. Columnar grains only grow competitively for a short time as they don't cross the layers and have to start growing again each time. It also impacts grain size and texture, as the preferred growth direction (001) does not have time to appear in a single layer. Therefore, the microstructure obtained with a strategy including active cooling results in a fine, lightly textured microstructure, whose mechanical properties are undoubtedly closer to those derived from an equiaxed rather than a columnar microstructure. This result was achieved regardless of the parameters chosen within the machine's operating range.

To obtain this type of fine, mixed microstructure without additional equipment, it is necessary either to lower the energy level [17] or to add a time delay [19], both reducing productivity. However, active cooling presents the advantage of obtaining similar microstructures without time delay and regardless of process parameters. This improves process efficiency as process parameters can be chosen to optimize productivity instead of being conditioned by the desired microstructure.

4.2. Influence of process parameters on microstructure

The influence of scanning speed and laser power on the microstructure observed in this work is valid in the specific case of grains not crossing the layers. Otherwise, the results may not be applicable. Quantitative analysis of the samples revealed a correlation between scanning speed and columnar grain size, regardless of power. As the grains do not pass through the layers, grain size is limited by the size of the beads. However, bead size is inversely proportional to scanning speed. Increasing speed produces smaller beads and, on average, smaller grains.

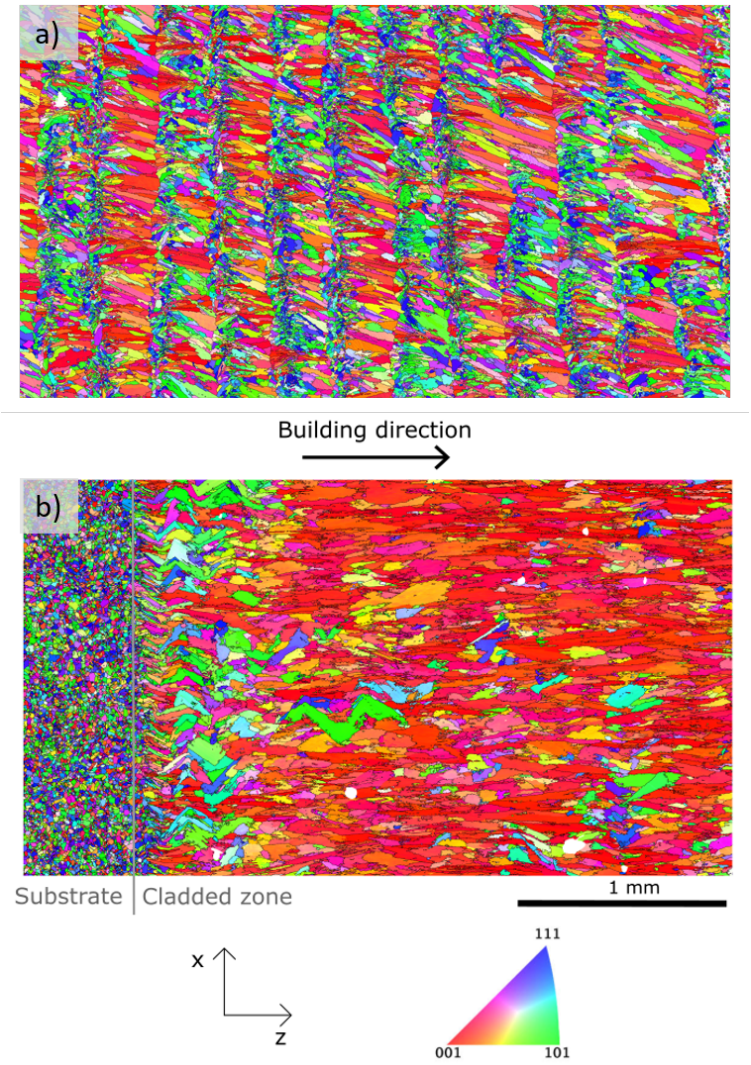

Figure 11: IPF in the building direction (a) unidirectional strategy with active cooling (b) bidirectional strategy of Guévenoux [38]

Scanning speed at constant power also has an impact on the tilt of the grains. As shown in figure 12, changing speed changes the shape of the melt pool. As speed decreases, the melt pool becomes deeper. Columnar grain growth follows the direction of the thermal gradient, i.e., perpendicular to the melt pool isotherm. By changing the speed and therefore the shape of the melt pool, the direction of the thermal gradient is also changed, and with it the direction of columnar grain growth. The angle between the substrate and the grains decreases as the melt pool becomes deeper, according to the shape of the isotherm. Thus, higher velocity results in more vertical grains.

Contrary to what can be found in the literature, in the case of wall production without active cooling, laser power has little impact on microstructure. For the same scanning speed, increasing the laser power induces an almost negligible increase of the average columnar grain size. Higher laser power indeed results in a higher thermal gradient in the melt pool, and as seen from the diagram in Figure 10(b), increasing the thermal gradient leads to a shift towards the fully columnar solidification regime. There is therefore a smaller part of the melt pool where the solidification regime is fully equiaxed. As a result, the proportion of small grains in a given layer decreases with increasing laser power. However, changing the laser power, within the permissible range of variation, does not modify the size of the melt pool and its thermal characteristics sufficiently to see a significant impact on the microstructure. Indeed, as long as the grains do not pass through the layers, only the scanning speed can slightly modify the size and tilt of the

columnar grains. However, these grains represent only a tiny percentage of all the grains in the samples.

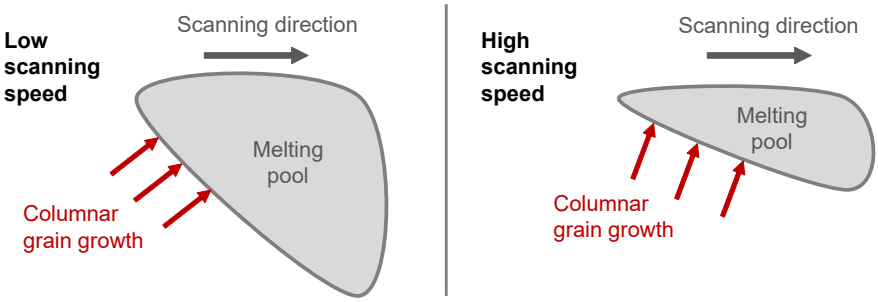

Figure 12: Scanning speed influence on grain inclination diagram

5. Conclusions and perspectives

This study proposes a new active cooling strategy to refine the microstructure and get closer to an equiaxed microstructure. With a unidirectional strategy, the nozzle passes over the deposit with the laser switched off, projecting the powder. In the case of the single-bead thin wall, this strategy produced a fine, untextured microstructure, irrespective of the process parameters. The structure consists of alternating columnar grains within a bead and small equiaxed grains between layers. Few grains can be seen passing through a layer, and the average grain size does not exceed 28.5 µm. A comparison of the microstructure obtained for a similar parameterization on the same machine highlights the significant contribution of active cooling. This active cooling strategy, therefore, improves process productivity as process parameters can be chosen to optimize productivity instead of being conditioned by the targeted microstructure.

Even under active cooling conditions, slightly modifying the already fine microstructure using scanning speed is possible. Increasing the scanning speed reduces the height of the beads and, therefore, the grain size and modifies the shape of the melt pool, leading to the growth of grains more aligned with the building direction. These changes are relatively minor compared with the impact of adding active cooling.

By using the nozzle to actively cool the part, it is possible to approach a fine equiaxed microstructure and the mechanical properties that go with it without the need for additional equipment. Out-of-production nozzle movements then become an essential part of the microstructure control strategy.

Declaration of competing interest

The authors declare that they have no known competing financial interests or personal relationships that could have appeared to influence the work reported in this paper.

Data availability

Data will be available upon request.

References

[1] ISO/ASTM 52900:2021, Additive manufacturing — General principles — Fundamentals and vocabulary, International Organization for Standardization, 2021.

[2] D. D. Gu, W. Meiners, K. Wissenbach, R. Poprawe, Laser additive manufacturing of metallic components: materials, processes and mechanisms, International Materials Reviews 57 (2012) 133–164.

[3] T. DebRoy, H. Wei, J. Zuback, T. Mukherjee, J. Elmer, J. Milewski, A. Beese, A. Wilson-Heid, A. De, W. Zhang, Additive manufacturing of metallic components - process, structure and properties, Progress in Materials Science 92 (2018) 112–224.
[4] V. P. E. Hosseini, A review of mechanical properties of additively manufactured inconel 718, Additive Manufacturing 30 (2019) 100877.
[5] B. Chen, J. Mazumder, Role of process parameters during additive manufacturing by direct metal deposition of inconel 718, Rapid Prototyping Journal 23 (2017) 919–929.
[6] Debroy, Physical processes in fusion welding, Reviews of Modern Physics 67 (1995) 85–112.
[7] D. Weisz-Patrault, Fast simulation of temperature and phase transitions in directed energy deposition additive manufacturing, Additive Manufacturing 31 (2020) 100990.
[8] A. Edwards, D. Weisz-Patrault, E. Charkaluk, Analysis and fast modelling of microstructures in duplex stainless steel formed by directed energy deposition additive manufacturing, Additive Manufacturing 61 (2023) 103300.
[9] L. Costa, R. Vilar, Laser powder deposition, Rapid prototyping journal 15 (2009) 264–279.
[10] D. Weisz-Patrault, S. Sakout, A. Ehrlacher, Fast simulation of temperature and grain growth in directed energy depostion additive manufacturing, in: 14th World Congress on Computational Mechanics, volume 1, ECCOMAS Congress, p. 2748.
[11] T. Blanc, Fabrication additive par dépôt laser direct de TA6V: étude expérimentale dans des régimes de forte productivité, modèles de comportement et recyclage de la poudre, Ph.D. thesis, Paris Sciences et Lettres (ComUE), 2017.
[12] T. W. E. J. W. Elmer, S. M. Allen, Microstructural development duringsolidification of stainless steel alloys, Metallurgical Transactions A 20 (1989) 2117–2131.
[13] J. D. Hunt, Steady state columnar and equiaxed growth of dendrites and eutectic, Materials Science and Engineering 65 (1984) 75–83.
[14] J. Maisonneuve, Fabrication directe de pièces aéronautiques en TA6V et IN718: Projection et fusion sélective par laser, Ph.D. thesis, Paris, ENMP, 2008.
[15] X. Ni, L. Zhang, W. Wu, D. Zhu, D. Kong, C. Dong, G. Zhu, Functionally nb graded inconel 718 alloys fabricated by laser melting deposition: mechanical properties and corrosion behavior, Anti-Corrosion Methods and Materials 67 (2019) 16–23.
[16] N. Sargent, Y. Wang, D. Li, Y. Zhao, X. Wang, W. Xiong, Exploring alloy design pathway through directed energy deposition of powder mixtures: A study of stainless steel 316l and inconel 718, Additive Manufacturing Letters 6 (2023) 100133.
[17] L. L. Parimi, R. G. A., D. Clark, M. M. Attallah, Microstructural and texture development in direct laser fabricated IN718, Materials Characterization 89 (2014) 102–111.
[18] E. Chauvet, C. Tassin, J.-J. Blandin, R. Dendievel, G. Martin, Producing ni-base superalloys single crystal by selective electron beam melting, Scripta Materialia 152 (2018) 15–19.
[19] C. Guévenoux, S. Hallais, A. Charles, E. Charkaluk, A. Constantinescu, Influence of interlayer dwell time on the microstructure of inconel 718 laser cladded component, Optics & Laser Technology 128 (2020) 106218.
[20] A. Yadollahi, N. Shamsaei, S. M. Thompson, D. W. Seely, Effects of process time interval and heat treatment on the mechanical and microstructural properties of direct laser deposited 316l stainless steel, Materials Science and Engineering: A 644 (2015) 171–183.
[21] M. Bambach, I. Sizova, F. Silze, M. Schnick, Comparison of laser metal deposition of inconel 718 from powder, hot and cold wire, Procedia CIRP 74 (2018) 206–209.
[22] G. Dinda, A. Dasgupta, J. Mazumder, Texture control during laser deposition of nickel-based superalloy, Scripta Materialia 67 (2012) 503–506.
[23] F. Liu, X. Lin, C. Huang, M. Song, G. Yang, J. Chen, W. Huang, The effect of laser scanning path on microstructures and mechanical properties of laser solid formed nickel-base superalloy inconel 718, Journal of Alloys and Compounds 509 (2011) 4505–4509.
[24] J. Cao, F. Liu, X. Lin, C. Huang, J. Chen, W. Huang, Effect of overlap rate on recrystallization behaviors of laser solid formed inconel 718 superalloy, Optics & Laser Technology 45 (2013) 228–235.
[25] V. Ocelík, I. Furár, J. D. Hosson, Microstructure and properties of laser clad coatings studied by orientation imaging microscopy, Acta Materialia 58 (2010) 6763–6772.

[26] S. J. Bremer, M. Luckabauer, G. willem R.B.E. Römer, Laser intensity profile as a means to steer microstructure of deposited tracks in directed energy deposition, Materials & Design 227 (2023) 111725.
[27] H. Xiao, S. Li, X. Han, J. Mazumder, L. Song, Laves phase control of inconel 718 alloy using quasi-continuous-wave laser additive manufacturing, Materials & Design 122 (2017) 330–339.
[28] Y. Zhou, W. Qu, F. Zhou, X. Li, L. Song, Q. Zhu, Thermo-fluid flow behavior of the in718 molten pool in the laser directed energy deposition process under magnetic field, Rapid Prototyping Journal 29 (2022) 460–473.
[29] C. Tan, R. Li, J. Su, D. Du, Y. Du, B. Attard, Y. Chew, H. Zhang, E. J. Lavernia, Y. Fautrelle, J. Teng, A. Dong, Review on field assisted metal additive manufacturing, International Journal of Machine Tools and Manufacture 189 (2023) 104032.
[30] F. Ning, Y. Hu, Z. Liu, W. Cong, Y. Li, X. Wang, Ultrasonic vibration-assisted laser engineered net shaping of inconel 718 parts: A feasibility study, Procedia Manufacturing 10 (2017) 771–778.
[31] X. Wang, A. Wang, Y. Li, A sequential path-planning methodology for wire and arc additive manufacturing based on a water-pouring rule, The International Journal of Advanced Manufacturing Technology 103 (2019) 3813–3830.
[32] Y. Zhou, W. Qu, F. Zhou, X. Li, L. Song, Q. Zhu, Thermo-fluid flow behavior of the in718 molten pool in the laser directed energy deposition process under magnetic field, Rapid Prototyping Journal 29 (2023) 460–473.
[33] Y. Zhang, Z. Li, P. Nie, Y. Wu, Effect of cooling rate on the microstructure of laser-remelted inconel 718 coating, Metallurgical and Materials Transactions A 44 (2013) 5513–5521.
[34] J. R. Davis, et al., Nickel, cobalt, and their alloys, ASM international, 2000.
[35] T. Zurcher, V. Fridrici, E. Charkaluk, Surface microstructure of an in718 3d coating manufactured by laser metal deposition, Materials Characterization (2023) 113054.
[36] M. Bréhier, D. Weisz-Patrault, C. Tournier, Revisiting the influence of the scanning speed on surface topography and microstructure of in718 thin walls in directed energy deposition additive manufacturing, Procedia CIRP 108 (2022) 470–476.
[37] L. Nastac, J. Valencia, M. Tims, F. Dax, Advances in the solidification of in718 and rs5 alloys, Superalloys 718 (2001) 625–706.
[38] C. Guevenoux, Réparation de pièces métalliques par Directed Energy Deposition : gradient microstructural, comportement mécanique et tenue en fatigue, Ph.D. thesis, 2021. Thèse de doctorat dirigée par Constantinescu, Andrei et Charkaluk, Éric Mécanique Institut polytechnique de Paris 2021.